PASJ: Publ. Astron. Soc. Japan **54**, 253–266, 2002 April 25

Super-Eddington Black-Hole Models for SS 433

Toru OKUDA
Hakodate College, Hokkaido University of Education, 1-2 Hachiman-cho, Hakodate 040-8567
okuda@cc.hokkyodai.ac.jp

(Received 2001 September 25; accepted 2002 January 7)

Abstract

We examine highly super-Eddington black-hole models for SS 433, based on two-dimensional hydrodynamical calculations coupled with radiation transport. The super-Eddington accretion flow with a small viscosity parameter, $\alpha = 10^{-3}$, results in a geometrically- and optically-thick disk with a large opening angle of $\sim 60^\circ$ to the equatorial plane and a very rarefied, hot, and optically-thin high-velocity jets region around the disk. The thick accretion flow consists of two different zones: an inner advection-dominated zone and an outer convection-dominated zone. The high-velocity region around the disk is divided into two characteristic regions, a very rarefied funnel region along the rotational axis and a moderately rarefied high-velocity region outside of the disk. The temperatures of $\sim 10^7$ K and the densities of $\sim 10^{-7}\,\mathrm{g\,cm^{-3}}$ in the upper disk vary sharply to $\sim 10^8$ K and $10^{-8}\,\mathrm{g\,cm^{-3}}$, respectively, across the disk boundary between the disk and the high-velocity region. The X-ray emission of iron lines would be generated only in a confined region between the funnel wall and the photospheric disk boundary, where flows are accelerated to relativistic velocities of $\sim 0.2\,c$ due to the dominant radiation-pressure force. The results are discussed regarding the collimation angle of the jets, the large mass-outflow rate observed in SS 433, and the ADAFs and the CDAFs models.

Key words: accretion, accretion disks — black hole physics — convection — hydrodynamics — stars: individual (SS 433)

1. Introduction

SS 433 is a very unusual and puzzling X-ray source, which exhibits remarkable observational features, such as two oppositely directed relativistic jets moving with a velocity of $0.26c$, its expected too-high energy, and a precessing motion of the jets over a period of 162.5 d. Although a number of papers concerning observational and theoretical data on SS 433 have been published (e.g., Margon 1984; Cherepashchuk 1993), the true nature of SS 433 is still not clear. Before the discovery of SS 433, Shakura and Sunyaev (1973) already discussed the observational appearance of a super-Eddington accretion disk around black holes. Regarding these points, many studies have been made concerning the relativistic jets of SS 433 (Katz 1980; Meier 1982; Lipunov, Shakura 1982) and its collimated ejection (Sikora, Wilson 1981; Begelman, Rees 1984). Thus, the super-Eddington accretion disks were generally expected to possess vortex funnels and radiation-pressure driven jets from geometrically-thick disks (Lynden-Bell 1978; Fukue 1982; Calvani, Nobili 1983). The radiative acceleration of particles near to the disk was also studied by several authors (Bisnovatyi-Kogan, Blinnikov 1977; Icke 1980, 1989; Fukue 1996; Tajima, Fukue 1998). A two-dimensional hydrodynamical calculation of a super-Eddington accretion disk around a black hole was first examined by Eggum et al. (1985, 1988), and was discussed regarding SS 433. They showed a relativistic jet formation just outside a conical photosphere of the accretion disk and a collimation angle of $\sim 30^\circ$ of the jet, where the dominant radiation-pressure force accelerates the jet to about $1/3\,c$. However, the jet's mass flux is only 0.4% of the input accretion rate and is too small for SS 433.

Kotani et al. (1996) strongly suggested that SS 433 is a binary system under a highly super-Eddington regime of accretion, where the mass-outflow rate of SS 433 jets is restricted to be $\gtrsim 5 \times 10^{-7}\,M_\odot\,\mathrm{yr}^{-1}$, combining spectral X-ray observations of iron emission lines with hydrodynamical modeling. Brinkmann and Kawai (2000) have modeled the two-dimensional hydrodynamical outflow of the SS 433 jets, while developing their previous model of conically out-flowing jets, and discussed the relationship between the physical parameters of SS 433 jets and observationally accessible data.

Blandford and Begelman (1999) investigated an adiabatic inflow–outflow solution of the accretion disk, where the super-Eddington flow leads to a powerful wind. King and Begelman (1999) discussed the super-Eddington mass transfer in binary systems and how to accrete in such super-Eddington accretion disks. Furthermore, recent theoretical studies and two-dimensional simulations of the black holes accretion flows (Igumenshchev, Abramowicz 1999; Stone et al. 1999; Narayan et al. 2000; Quataert, Gruzinov 2000; Stone, Pringle 2001; Abramowicz et al. 2001) showed a new development in the advection-dominated accretion flows (ADAFs) and the convection-dominated accretion flows (CDAFs) which may be deeply related to the super-Eddington accretion flows. Okuda and Fujita (2000) have examined the super-Eddington accretion disk model of a neutron star for SS 433 by two-dimensional hydrodynamical calculations and discussed the characteristics of the super-Eddington flows. In this paper, following the neutron star model, we examine the super-Eddington black-hole models and discuss the results regarding SS 433 and also AVAFs and CDAFs.

2. Model Equations

A set of relevant equations consists of six partial differential equations for density, momentum, and thermal and radiation energy. These equations include the full viscous stress tensor, heating and cooling of the gas, and radiation transport. The radiation transport is treated in the gray, flux-limited diffusion approximation (Levermore, Pomraning 1981). We use spherical polar coordinates (r, ζ, φ), where r is the radial distance, ζ is the polar angle measured from the equatorial plane of the disk, and φ is the azimuthal angle. The gas flow is assumed to be axisymmetric with respect to Z-axis ($\partial/\partial\varphi = 0$) and the equatorial plane . In this coordinate system, the basic equations for mass, momentum, gas energy, and radiation energy are written in the following conservative form (Kley 1989):

$$\frac{\partial \rho}{\partial t} + \mathrm{div}(\rho \boldsymbol{v}) = 0, \tag{1}$$

$$\frac{\partial(\rho v)}{\partial t} + \mathrm{div}(\rho v \boldsymbol{v}) = \rho\left[\frac{w^2}{r} + \frac{v_\varphi^2}{r} - \frac{GM_*}{(r-r_\mathrm{g})^2}\right] - \frac{\partial p}{\partial r} + f_r + \mathrm{div}\boldsymbol{S}_r + \frac{1}{r}S_{rr}, \tag{2}$$

$$\frac{\partial(\rho r w)}{\partial t} + \mathrm{div}(\rho r w \boldsymbol{v}) = -\rho v_\varphi^2 \tan\zeta - \frac{\partial p}{\partial \zeta} + \mathrm{div}(r\boldsymbol{S}_\zeta) + S_{\varphi\varphi}\tan\zeta + f_\zeta, \tag{3}$$

$$\frac{\partial(\rho r \cos\zeta\, v_\varphi)}{\partial t} + \mathrm{div}(\rho r \cos\zeta\, v_\varphi \boldsymbol{v}) = \mathrm{div}(r\cos\zeta \boldsymbol{S}_\varphi), \tag{4}$$

$$\frac{\partial \rho\varepsilon}{\partial t} + \mathrm{div}(\rho\varepsilon\boldsymbol{v}) = -p\,\mathrm{div}\boldsymbol{v} + \Phi - \Lambda, \tag{5}$$

and

$$\frac{\partial E_0}{\partial t} + \mathrm{div}\boldsymbol{F}_0 + \mathrm{div}(\boldsymbol{v}E_0 + \boldsymbol{v}\cdot P_0) = \Lambda - \rho\frac{(\kappa+\sigma)}{c}\boldsymbol{v}\cdot\boldsymbol{F}_0, \tag{6}$$

where ρ is the density, $\boldsymbol{v} = (v, w, v_\varphi)$ are the three velocity components, G is the gravitational constant, M_* is the central mass, p is the gas pressure, ε is the specific internal energy of the gas, E_0 is the radiation energy density per unit volume, and P_0 is the radiative stress tensor. It should be noticed that the subscript "0" denotes the value in the comoving frame and that the equations are correct to the first order of $\boldsymbol{v}/c$ (Kato et al. 1998). We adopt the pseudo-Newtonian potential (Paczyński, Wiita 1980) in equation (2), where r_g is the Schwarzschild radius. The force density $\boldsymbol{f}_\mathrm{R} = (f_r, f_\zeta)$ exerted by the radiation field is given by

$$\boldsymbol{f}_\mathrm{R} = \rho\frac{\kappa+\sigma}{c}\boldsymbol{F}_0, \tag{7}$$

where κ and σ denote the absorption and scattering coefficients and $\boldsymbol{F}_0$ is the radiative flux in the comoving frame. $S = (\boldsymbol{S}_r, \boldsymbol{S}_\zeta, \boldsymbol{S}_\varphi)$ denote the viscous stress tensor. $\Phi = (S\,\nabla)\boldsymbol{v}$ is the viscous dissipation rate per unit mass.

The quantity Λ describes the cooling and heating of the gas, i.e., the energy exchange between the radiation field and the gas due to absorption and emission processes,

$$\Lambda = \rho c\kappa(S_* - E_0), \tag{8}$$

where S_* is the source function and c is the speed of light. For this source function, we assume local thermal equilibrium $S_* = aT^4$, where T is the gas temperature and a is the radiation constant. For the equation of state, the gas pressure is given by the ideal gas law, $p = R_\mathrm{G}\rho T/\mu$, where μ is the mean molecular weight and R_G is the gas constant. The temperature T is proportional to the specific internal energy, ε, by the relation $p = (\gamma-1)\rho\varepsilon = R_\mathrm{G}\rho T/\mu$, where γ is the specific heat ratio. To close the system of equations, we use the flux-limited diffusion approximation (Levermore, Pomraning 1981) for the radiative flux:

$$\boldsymbol{F}_0 = -\frac{\lambda c}{\rho(\kappa+\sigma)}\mathrm{grad}\,E_0, \tag{9}$$

and

$$P_0 = E_0 \cdot T_\mathrm{Edd}, \tag{10}$$

where λ and T_Edd are the *flux-limiter* and the *Eddington Tensor*, respectively, for which we use the approximate formulas given in Kley (1989). The formulas fulfill the correct limiting conditions in the optically-thick diffusion limit and the optically-thin streaming limit, respectively.

For the kinematic viscosity, ν, we adopt a modified version (Papaloizou, Stanley 1986; Kley, Lin 1996) of the standard α-model. The modified prescription for ν is given by

$$\nu = \alpha c_\mathrm{s} \min\left[H_\mathrm{p}, H\right], \tag{11}$$

where α is a dimensionless parameter, usually $\alpha = 0.001$–1.0, c_s the local sound speed, H the disk height, and $H_\mathrm{p} = p/|\mathrm{grad}\,p|$ the pressure scale height on the equatorial plane.

3. Numerical Methods

The set of partial differential equations (1)–(6) is numerically solved by a finite-difference method under initial and boundary conditions. The numerical schemes used are basically the same as that described by Kley (1989) and Okuda et al. (1997). The methods are based on an explicit–implicit finite difference scheme. N_r grid points (= 150) in the radial direction are spaced logarithmically, while N_ζ grid points (=100) in the angular direction are equally spaced, but more refined near the equatorial plane, typically $\Delta\zeta = \pi/150$ for $\pi/2 \geq \zeta \geq \pi/6$ and $\Delta\zeta = \pi/300$ for $\pi/6 \geq \zeta \geq 0$.

3.1. Model Parameters

For the central star of SS 433, we assume a Schwarzschild black hole with mass $M_* = 10\,M_\odot$ and examine the structure and dynamics of an accretion disk around the black hole and its surrounding atmosphere. From an observational constraint of the mass-outflow rate, $\dot{M}_\mathrm{loss}$, of $\geq 5\times10^{-7}\,M_\odot\,\mathrm{yr}^{-1}$ ($3\times10^{19}\,\mathrm{g\,s}^{-1}$) in SS 433 (Kotani et al. 1996), we adopt a mass accretion rate $\dot{M}_*$ of $8\times10^{19}\,\mathrm{g\,s}^{-1}$, which corresponds to $\sim 4\dot{M}_\mathrm{E}$, where $\dot{M}_\mathrm{E}$ is the Eddington critical accretion rate for the black hole, given by

$$\dot{M}_\mathrm{E} = \frac{48\pi GM_*}{\kappa_\mathrm{e}c}, \tag{12}$$

where κ_e is the electron scattering opacity.

For the viscosity parameter, α, we consider two cases, 10^{-3} (BH-1) and 0.1 (BH-2). The inner-boundary radius, R_*, of

Table 1. Model parameters.

Model	$M_*/M_\odot$	$\dot{M}_*/\dot{M}_{\rm E}$	$\dot{M}_*$ (g s^{-1})	α	R_*	$R_{\rm max}/R_*$
BH-1	10	4	8×10^{19}	10^{-3}	$2r_{\rm g}$	220
BH-2	10	4	8×10^{19}	0.1	$2r_{\rm g}$	220

the computational domain is taken to be $2r_{\rm g}$ and the outer-boundary radius, $R_{\rm max}$, is selected so that the radiation pressure is comparable to the gas pressure at the outer boundary, where the Shakura–Sunyaev instability never occurs. The model parameters used are listed in table 1.

3.2. Boundary and Initial Conditions

Physical variables at the inner boundary, except for the velocities, are given by extrapolation of the variables near the boundary. However, for the velocities, we impose limited conditions that the radial velocities are always negative and the angular velocities are zero. If the radial velocity by the extrapolation is positive, it is set to be zero; that is, outflow at the inner boundary is prohibited. On the rotational axis and the equatorial plane, the meridional tangential velocity w is zero and all scalar variables must be symmetric relative to these axes.

The outer boundary at $r = R_{\rm max}$ is divided into two parts. One is the disk boundary through which matter is entering from the outer disk. At the outer-disk boundary we assume a continuous inflow of matter with a constant accretion rate, $\dot{M}_*$. The other is the outer boundary region above the accretion disk. We impose free-floating conditions on this outer boundary (i.e., all gradients vanish) and allow for outflow of matter, whereas any inflow is prohibited here. We also assume the outer boundary region above the disk to be in the optically-thin limit, $|\boldsymbol{F}_0| \to cE_0$. This imposes a boundary condition on the radiation energy density, E_0. The initial configuration consists of a cold, dense, and optically-thick disk and a hot, rarefied, and optically-thin atmosphere around the disk. The initial disk is approximated by the Shakura–Sunyaev's standard model. The initial hot rarefied atmosphere around the disk is constructed to be approximately in hydrostatic equilibrium.

4. Results

4.1. Model BH-1 with $\alpha = 10^{-3}$

The initial disk thickness, H/r, based on the standard disk model, is ~ 1 at the inner region and ~ 0.1 at the outer boundary. The ratio β of the gas pressure to the total pressure at the initial outer disk boundary is ~ 0.27. We performed a time evolution of the disk until $t = 4\times10^3 P_{\rm d}$ for model BH-1, where $P_{\rm d}$ is the Keplerian orbital period at the inner boundary.

Figure 1 shows the time evolution of the total luminosity, L, for model BH-1. After an initial sharp rise of the luminosity, the luminosity curve descends gradually toward a steady state value. The luminosity L at the final phase is 1.6×10^{39} erg s^{-1} and $L/L_{\rm E}$ is ~ 1, which is far smaller than $\dot{M}_*/\dot{M}_{\rm E}\,(=4)$, where $L_{\rm E}$ is the Eddington luminosity.

At the initial stage of the evolution, matter in the inner region of the disk is ejected strongly outward. Some of the ejected gas hit on the rotational axis and others propagate outward.

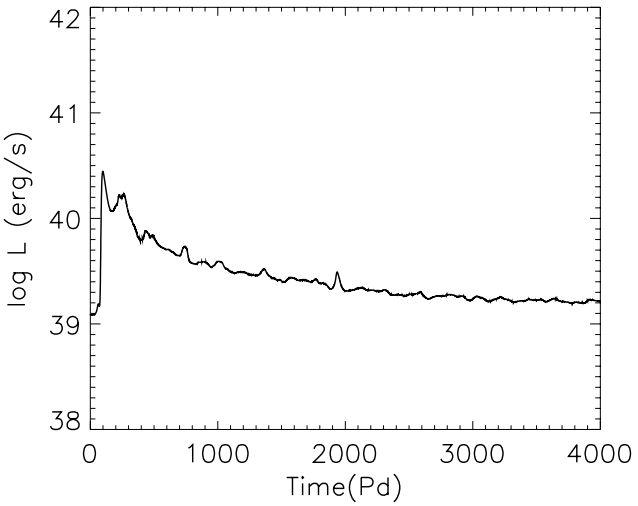

Fig. 1. Time evolution of the luminosity, L, for model BH-1, where $P_{\rm d}$ is the Keplerian orbital period at the inner boundary $2r_{\rm g}$.

The gas hitting on the axis leads to a high-temperature region along the axis and anisotropic radiation fields, in which equi-contour lines of the radiation energy density are concentric. This results in an outward radiation-pressure force, which dominates the gravitational force, and a high-velocity jet region is formed along the axis. At the beginning of the evolution, the high-velocity region is confined to a narrow region along the rotational axis, but gradually spreads outward from the axis. The spreading-jet gas interacts with the surrounding medium and finally settles down to a quasi-steady state. On the other hand, the initially optically thin atmosphere above the initial disk is occupied by the dense gas ejected from the inner disk with increasing time, and becomes optically thick at the final phase, forming a cone-like shape with a large opening angle of $\sim 60^\circ$ to the equatorial plane. We regard this optically-thick and dense region as an accretion disk. The boundary between the high-velocity region and the disk is characterized by sharp gradients of density and temperature.

In order to understand well the evolution of the disk and the high-velocity region, we animated the density and temperature evolutions. Figure 2 denotes nine snapshots of the density evolution, where the right-hand number in each snap shows the evolutionary time in units of $P_{\rm d}$; also, a color legend for $\log\rho$ (g cm^{-3}) is shown. The green and orange parts in the later snaps express the rarefied, hot, and optically thin high-velocity jets region, while the blue and dark blue parts denote the optically-thick and dense disk region. In the high-velocity region, we distinguish the orange region (which we call the funnel region) from the green region, because the densities in the orange region decrease sharply towards the rotational axis

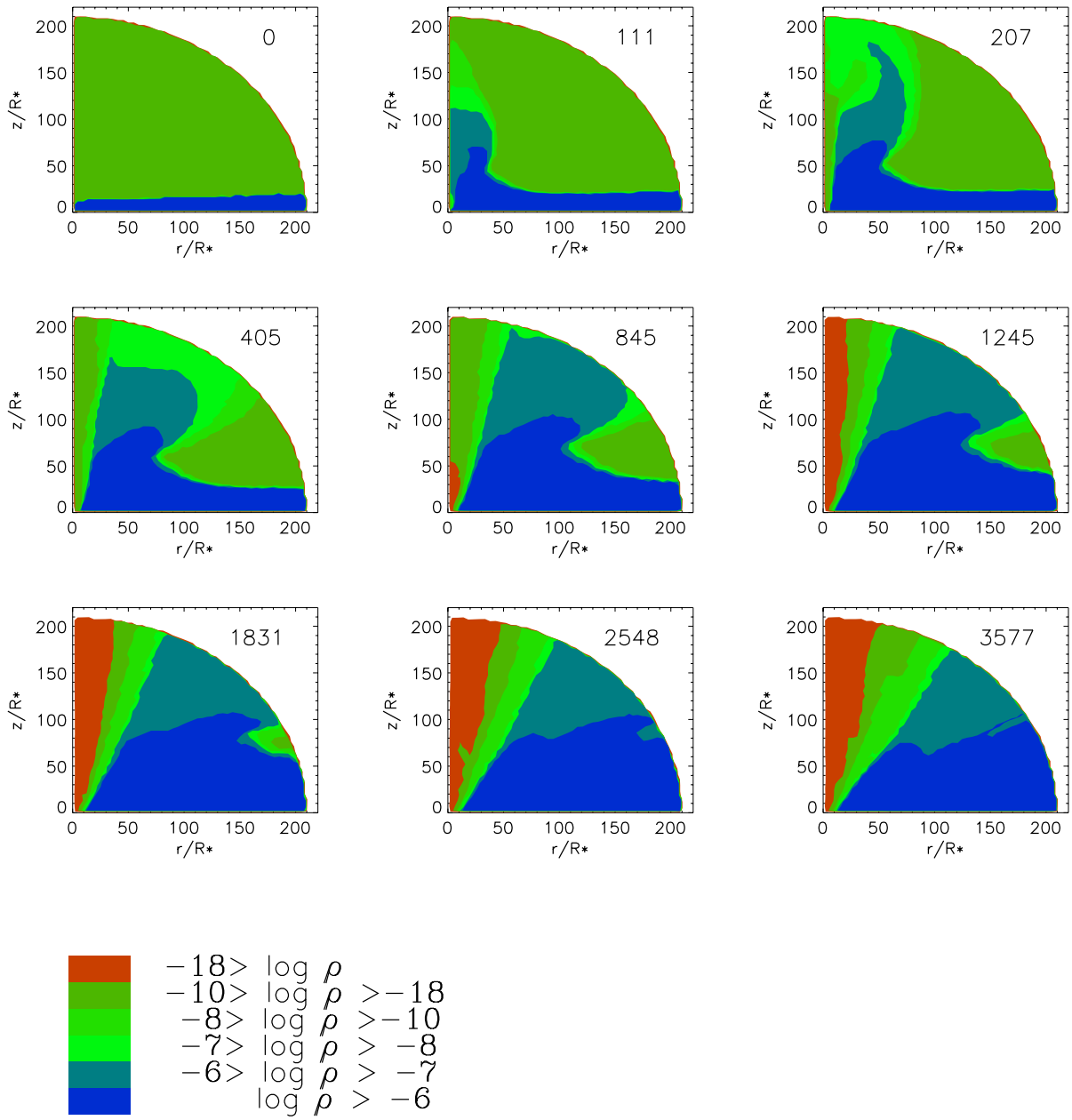

Fig. 2. Snapshots of the density evolution for model BH-1, where the right-hand number in each photo shows the evolutionary time in units of $P_{\rm d}$; also, a color legend for $\log \rho$ (g cm^{-3}) is shown. The first snapshot denotes the initial density configurations, which consist of the Shakura–Sunyaev disk and the surrounding rarefied atmosphere. The green and orange parts in the later snaps show the hot, rarefied, and optically-thin high-velocity jets region, while the blue and dark blue parts denote the cold, dense, and optically-thick disk region. The flow velocities at the final phase are ~ 0.1–$0.2\,c$ in the deep-green part and ~ 0.2–$0.4\,c$ in the light-green and orange parts. The observed X-ray emission of iron lines in SS 433 would be formed in the deep-green high-velocity region just outside the disk boundary.

and are as very low as 10^{-18}–10^{-26} g cm^{-3}, compared with 10^{-8}–10^{-18} g cm^{-3} in the green region. Therefore, we have three characteristic regions here: (A) the disk region (blue), (B) the high-velocity region (green), and (C) the very rarefied funnel region (orange). As discussed later, the centrifugal barrier and the funnel wall lie near the boundaries, between (A) and (B), and between (B) and (C) at the final phase, respectively.

Figure 3 shows the density contours with velocity vectors (a) and the temperature contours (b) on the meridional plane at $t = 3577 P_{\rm d}$. In figure 3a, the density contours are denoted by the labels $\log \rho = -5$, -6, -7, -8 ,-10, and -18. The velocity vectors show the maximum velocity, $0.4\,c$, at $\zeta \sim 80^\circ$ and $r/R_* \sim 200$. The thick dot-dashed line in (a) shows the disk boundary between the disk and the high-velocity region. Here, we approximately define the disk boundary as an interface through which a temperature of $\sim 10^7$ K in the disk jumps to $\sim 10^8$ K. The disk boundary lies roughly between the density labels -7 and -8. In the funnel region (C) ($\zeta \gtrsim 80^\circ$), the

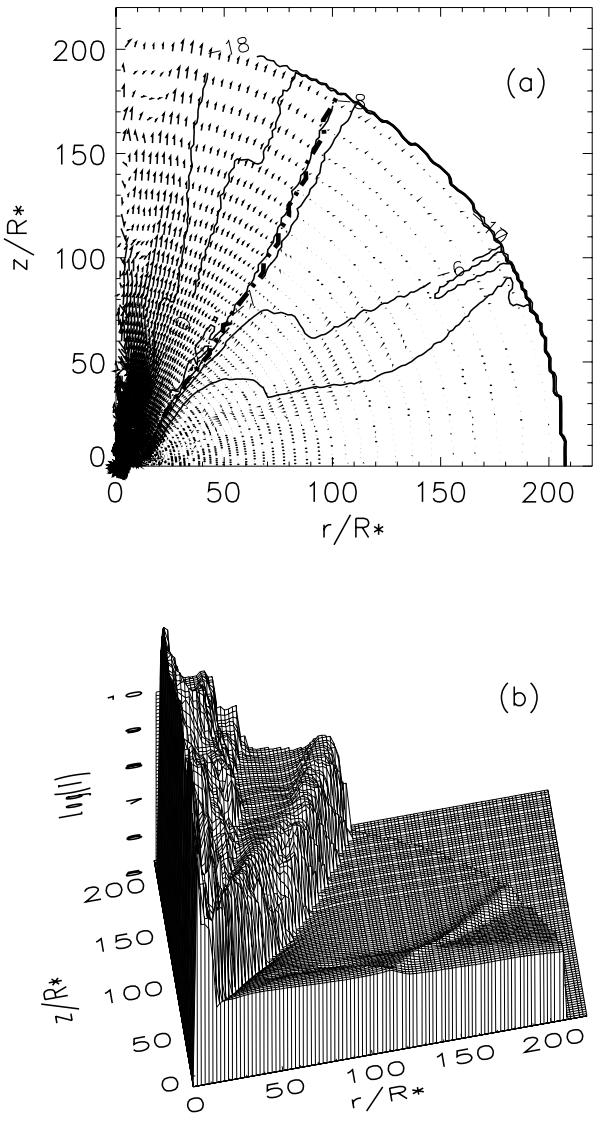

Fig. 3. Velocity vectors and contours of the density, ρ (g cm^{-3}), in logarithmic scale (a) and a bird's-eye view of the gas temperature T (K) (b), on the meridional plane at the evolutionary time $t = 3577\,P_{\rm d}$ for model BH-1. The density contours are denoted by the labels $\log\rho = -5$, -6, -7, -8, -10, and -18, and the velocity vectors show the maximum velocity $0.4\,c$ at $\zeta \sim 80°$ and $r/R_* \sim 200$. The thick dot-dashed line in (a) shows the disk boundary between the disk and the high-velocity region.

flow velocities are very large, but rather chaotic near the rotational axis. In the high-velocity region (B) ($80° \gtrsim \zeta \gtrsim 60°$), the flows are relativistic to be ~ 0.1–$0.2\,c$, and the gas streams run radially. Figure 3b shows a bird's-eye view of the temperature, where the disk boundary is clearly recognized by a sharp wall with high temperatures. The temperatures range from 2×10^6 to $\sim 10^7$ K in the disk region, jump to $\sim 10^8$ K just across the disk boundary, and again distribute gradually between $\sim 10^8$ and 10^9 K in the high-velocity region. In the funnel region near the rotational axis, the temperatures are as very high as $\sim 10^9$–10^{11} K. On the mid-plane, the densities and the temperatures are not largely different from the initial ones, except for the innermost region of $r/R_* \lesssim 10$, where the flow is more rarefied and hotter than the initial flow.

Figure 4 shows the contours of radiation energy density, E_0, in an arbitrary unit (a) and angular-velocity Ω (b) on the meridional plane at $t = 3577\,P_{\rm d}$, where the thick dot-dashed line denotes the disk boundary. In figure 4a, E_0 is almost independent on ζ in the optically-thin high-velocity region and weakly dependent on ζ in the upper disk region, and so the radiation-pressure gradient forces act only radially in the high-velocity region (B). In figure 4b, the angular velocities, Ω, in unit of the Keplerian angular velocity at the inner boundary are denoted by the contours of $\log\Omega$. The angular velocities show two kinds of characteristic distributions. Near to the equatorial plane, the angular velocities are nearly Keplerian. However, in the upper disk and the high-velocity region, the equi-contours of Ω are parallel to the Z-axis, and Ω behaves approximately as $K/x^{2.1}$, where x is the distance in units of $2\,r_{\rm g}$ from the Z-axis and K is a constant, although the constant K seems to change slightly on the disk boundary and the funnel wall. As a result, the specific angular momentum $\lambda_{\rm a}$ ($= x^2\Omega$) is approximately conserved in these regions. From the numerical data, we find $\Omega = 5.6/x^{2.1}$ with our non-dimensional units in the high-velocity region. The funnel wall, a barrier where the effective potential due to the gravitational potential and the centrifugal one vanishes, is described by a surface $(x_{\rm f}, z_{\rm f})$,

$$(\Phi)_{\rm eff} = \frac{-1}{(r_{\rm f} - 1/2)} + \frac{\lambda_{\rm a}^2}{2x_{\rm f}^3} = 0, \tag{13}$$

where $r_{\rm f} = (x_{\rm f}^2 + z_{\rm f}^2)^{1/2}$ is given in units of $2\,r_{\rm g}$ (Molteni et al. 1996). From equation (13) together with the above Ω, the funnel wall is shown by the thick dashed line in figure 4b. The funnel region (C) and the high-velocity region (B) are roughly separated by the funnel wall.

The acceleration for the relativistic flows depends on the distribution of the radiation pressure, $P_{\rm r}$ ($= f_{\rm E}E_0$), where $f_{\rm E}$ is the Eddington factor. The flux limiter, λ, almost equals to $1/3$ in the optically-thick disk, while in the optically-thin high-velocity region, λ is very small and its spatial variation is almost identical to that of the density, ρ. In regions (B) and (C), the radiation temperatures, $T_{\rm r} = (E_0/a)^{1/4}$, depend almost only on r and are small compared with the gas temperature, T; also, the gas temperatures in the region (C) are much higher than that in the region (B). However, its too high temperature ($\sim 10^9$–10^{11} K) in region (C) may be unreliable because we did not take account of other physical processes, such as Compton processes and pair production–annihilation, which may be important at such high temperatures. On the other hand, we consider that the densities would not be drastically altered by the processes.

The radiation pressures are very dominant everywhere, especially in the inner region of the disk. In the disk region (A), the centrifugal forces balance the gravitational forces near to the disk midplane, whereas, at the upper disk region, the balances due to the centrifugal, the gravitational, and the radiation-pressure gradient forces are maintained. In regions (B) and (C), the dominant radial radiation-pressure forces are one order of magnitude larger than the gravitational forces because the densities in these regions are very low. As a result, the radiation-pressure gradient forces accelerate the flows radially

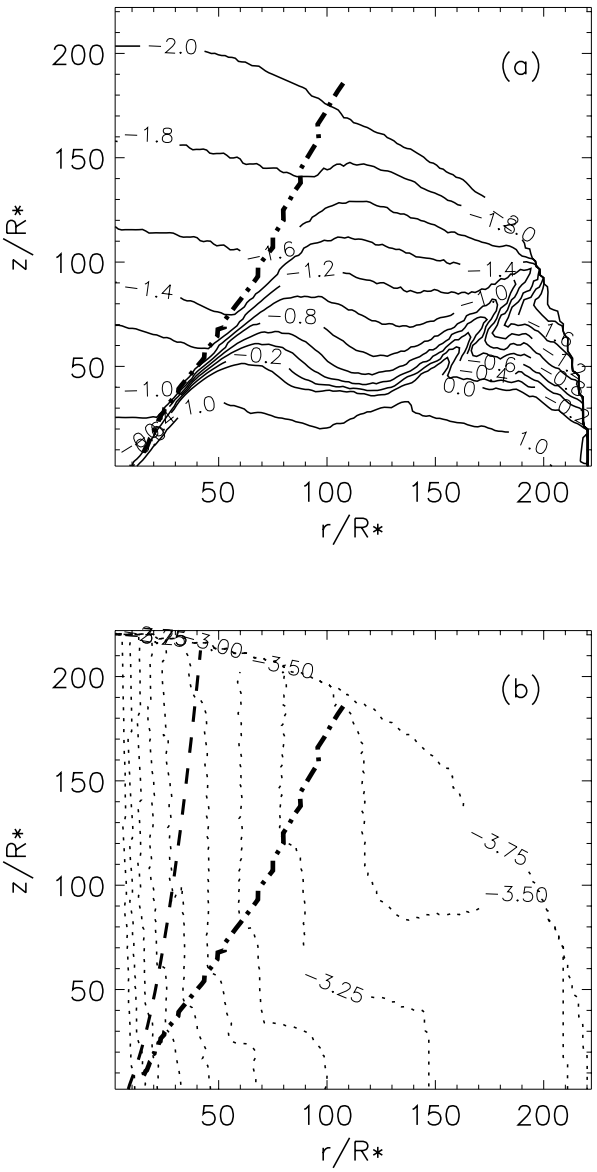

Fig. 4. Contours of the logarithmic radiation energy density $\log E_0$ in an arbitrary unit (a) and the logarithmic angular-velocity $\log\Omega$ normalized by the Keplerian angular velocity at the inner boundary with intervals of 0.25 (b) on the meridional plane at $t = 3577\,P_{\rm d}$ for model BH-1, where the thick dashed and the thick dot-dashed lines denote the funnel wall and the disk boundary between the disk and the high-velocity jets region, respectively.

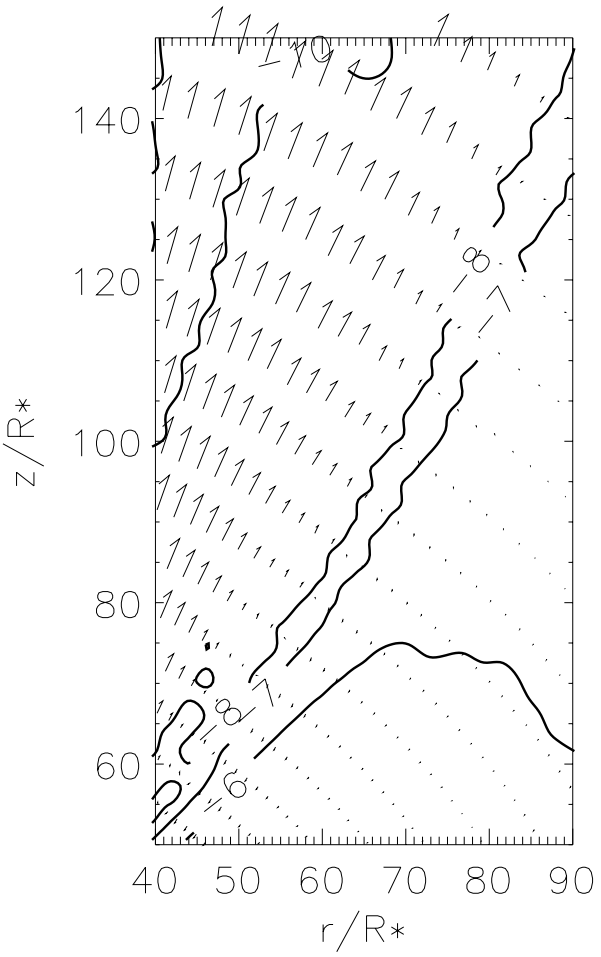

Fig. 5. Magnified velocity fields and density contours near the upper disk boundary at $t = 3577\,P_{\rm d}$ for model BH-1, where the maximum velocity is $0.22\,c$ and the contours of $\log\rho$ (g cm^{-3}) is shown by lines with labels -6, -7, -8, and -10. This high-velocity region above the disk boundary is a typical X-ray emitting region of iron lines with velocities of $\sim 0.2\,c$.

to relativistic velocities. The azimuthal velocities in the high-velocity region are in the range of 0.1–0.2 c, and the high-velocity gas is blown off spirally and relativistically. At the disk boundary between regions (A) and (B), the gravitational force balances roughly the radial component of centrifugal force, i.e., the boundary region corresponds to what is called a centrifugal barrier.

Figure 5 shows magnified velocity fields and the density contours near the upper disk boundary at $t = 3577\,P_{\rm d}$, where the maximum velocity is $0.22c$ and the contours of $\log\rho$ (g cm^{-3}) is shown by lines with labels -6, -7, -8, and -10. The disk boundary between regions (A) and (B) is between the density labels -7 and -8. As mentioned later, this high-velocity region above the disk boundary would correspond to a typical X-ray emitting region of iron lines with velocities of $\sim 0.2\,c$.

Figure 6 shows the flow features in the inner disk and the surrounding high-velocity region, where the velocities are indicated by unit vectors and the thick dot-dashed line shows the disk boundary. One of the remarkable features of luminous accretion disks is convective phenomena in the inner region of the disk (Eggum et al. 1985, 1988; Milsom, Taam 1997; Fujita, Okuda 1998). The convective motions are clearly found in this figure, and there appear more than a dozen of convective cells.

Previously it has been shown that a luminous accretion disk with $\dot{M}_* \sim \dot{M}_{\rm E}$ is unstable against convection, and that this is induced by a large negative gradient of entropy vertical to the equatorial plane (Bisnovatyi-Kogan, Blinnikov 1977; Fujita, Okuda 1998). The accretion flow is severely disrupted by the convective eddies. Recent theoretical studies and two-dimensional hydrodynamical simulations of radiatively inefficient black hole accretion flows (Stone et al. 1999; Igumenshchev, Abramowicz 1999; Narayan et al. 2000;

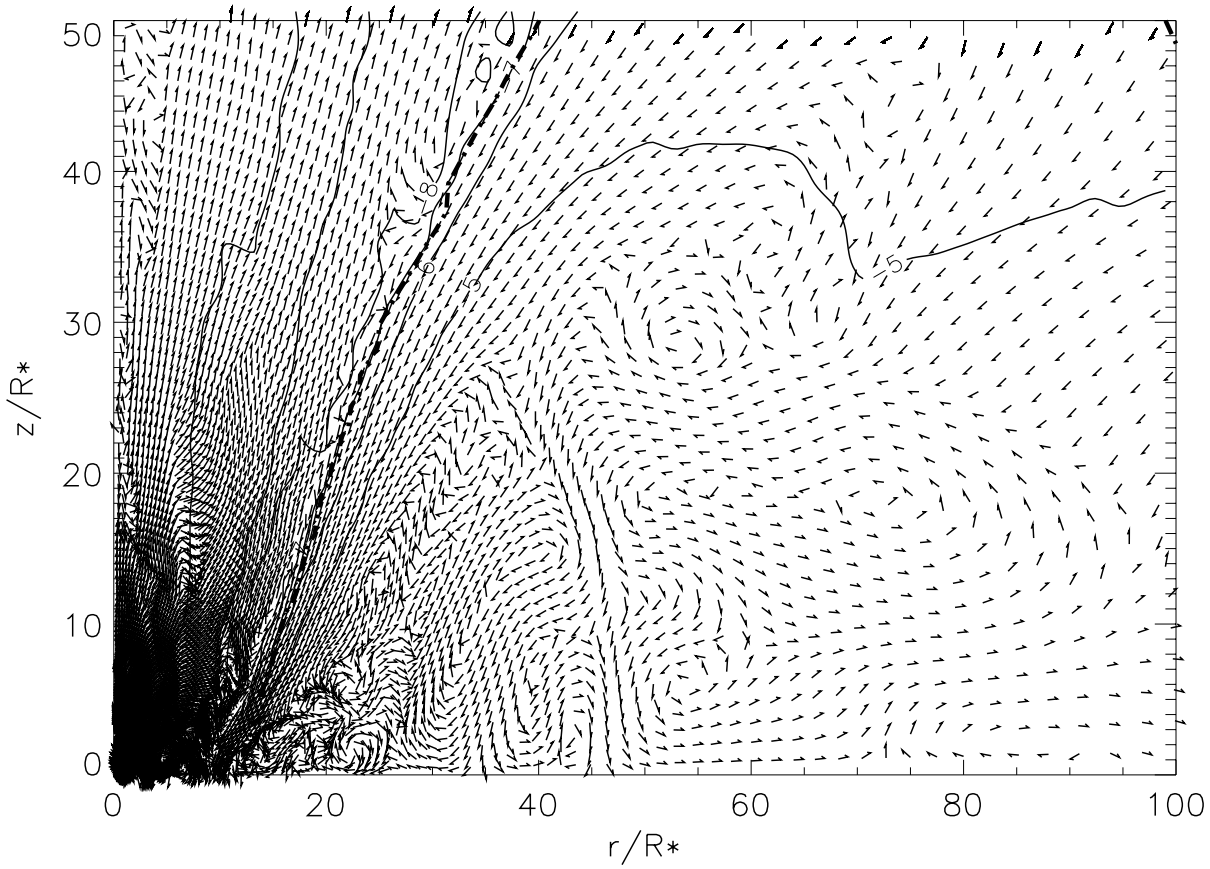

Fig. 6. Unit-velocity vectors and density contours of $\log\rho = -5$, -6, -7, -8, -10, and -18 in the inner disk and the surrounding high-velocity jets region at $t = 3577\,P_{\rm d}$ for model BH-1, where the dot-dashed line denotes the disk boundary between the disk and the high-velocity jets region. A transition between the inner advection-dominated zone and the outer convection-dominated zone occurs at $r \sim 10R_*$ ($= 20\,r_{\rm g}$).

Quataert, Gruzinov 2000) showed that accretion flows with low viscosities are generally convection-dominated flows (ADAFs and CDAFs) and have characteristic self-similar solutions of the disk variables which are described by power law profiles with radius. This was also confirmed in recent magneto-hydrodynamical simulations of the accretion flows around black holes (Stone, Pringle 2001).

Model BH-1 belongs to a typical ADAFs or a CDAFs case because of its small value of the viscosity parameter, α. Figure 7 denotes the radial and angular profiles of the time-averaged flow variables near the equatorial plane for model BH-1: (a) density, ρ, in units of ρ_0 ($= 10^{-8}\,{\rm g\,cm^{-3}}$); (b) radial velocity, v, in units of Keplerian velocity $v_{\rm K_*}$ at $r = R_*$; (c) total pressure, $P_{\rm t}$, in units of $\rho_0 v_{\rm K_*}^2$; (d) rotational velocity, v_φ (solid line), in units of $v_{\rm K_*}$ and the Keplerian one (dotted line); (e) radial mass-inflow rate, $\dot{M}_{\rm in}(r)$ (${\rm g\,s^{-1}}$) (solid line), mass-outflow rate, $\dot{M}_{\rm out}(r)$ (dashed line), net mass accretion rate, $\dot{M}_{\rm a}(r)$ ($= \dot{M}_{\rm in} + \dot{M}_{\rm out}$) (dotted line), in the whole region, and mass-outflow rate $\dot{M}_{\rm jet}(r)$ ($\diamond$) in the jet region; (f) convective luminosity, $L_{\rm c} = \int F_{\rm c}(r)\,dS$ (${\rm erg\,s^{-1}}$); (g) entropy, S, at $\zeta \sim 0^\circ$ (solid line) and 42° (dotted line) in an arbitrary unit; and (h) angular profiles of mass-inflow rate, $\dot{M}_{\rm in}(\zeta)$ (${\rm g\,s^{-1}}$) (solid line), mass-outflow rate, $\dot{M}_{\rm out}(\zeta)$ (dashed line), and net mass-flow rate, $\dot{M}_{\rm p}$ ($= \dot{M}_{\rm in} + \dot{M}_{\rm out}$) ($\diamond$), where $F_{\rm c}$ in (f) is the convective energy flux given by Narayan et al. (2000) and its integral is taken within the disk region, and the ordinate scale in (h) shows $Sign(\dot{M})\log|\dot{M}|$. The time-averaged and angle-integrated mass inflow and outflow rates ($\dot{M}_{\rm in}$ and $\dot{M}_{\rm out}$, respectively) in figure 7e are defined as

$$\dot{M}_{\rm in}(r) = 4\pi r^2 \int_0^{\pi/2} \rho \min(v, 0)\cos\zeta\, d\zeta, \tag{14}$$

and

$$\dot{M}_{\rm out}(r) = 4\pi r^2 \int_0^{\pi/2} \rho \max(v, 0)\cos\zeta\, d\zeta. \tag{15}$$

For these rates, the net mass accretion rate is $\dot{M}_{\rm a} = \dot{M}_{\rm in} + \dot{M}_{\rm out}$. These mass-flux rates are actually regarded as those in the disk region, since $\dot{M}_{\rm jet}$ is a few orders of magnitude smaller than $\dot{M}_{\rm in}$, $\dot{M}_{\rm out}$, and $\dot{M}_{\rm a}$ in figure 7e. Similarly, $\dot{M}_{\rm in}(\zeta)$ and $\dot{M}_{\rm out}(\zeta)$ are defined as

$$\dot{M}_{\rm in}(\zeta) = 4\pi\cos\zeta \int_{R_*}^{R_{\rm max}} r\rho \min(w, 0)\, dr, \tag{16}$$

and

$$\dot{M}_{\rm out}(\zeta) = 4\pi\cos\zeta \int_{R_*}^{R_{\rm max}} r\rho \max(w, 0)\, dr. \tag{17}$$

Abramowicz et al. (2001) suggest that low-viscosity accretion flows around black holes consist of two zones: an inner

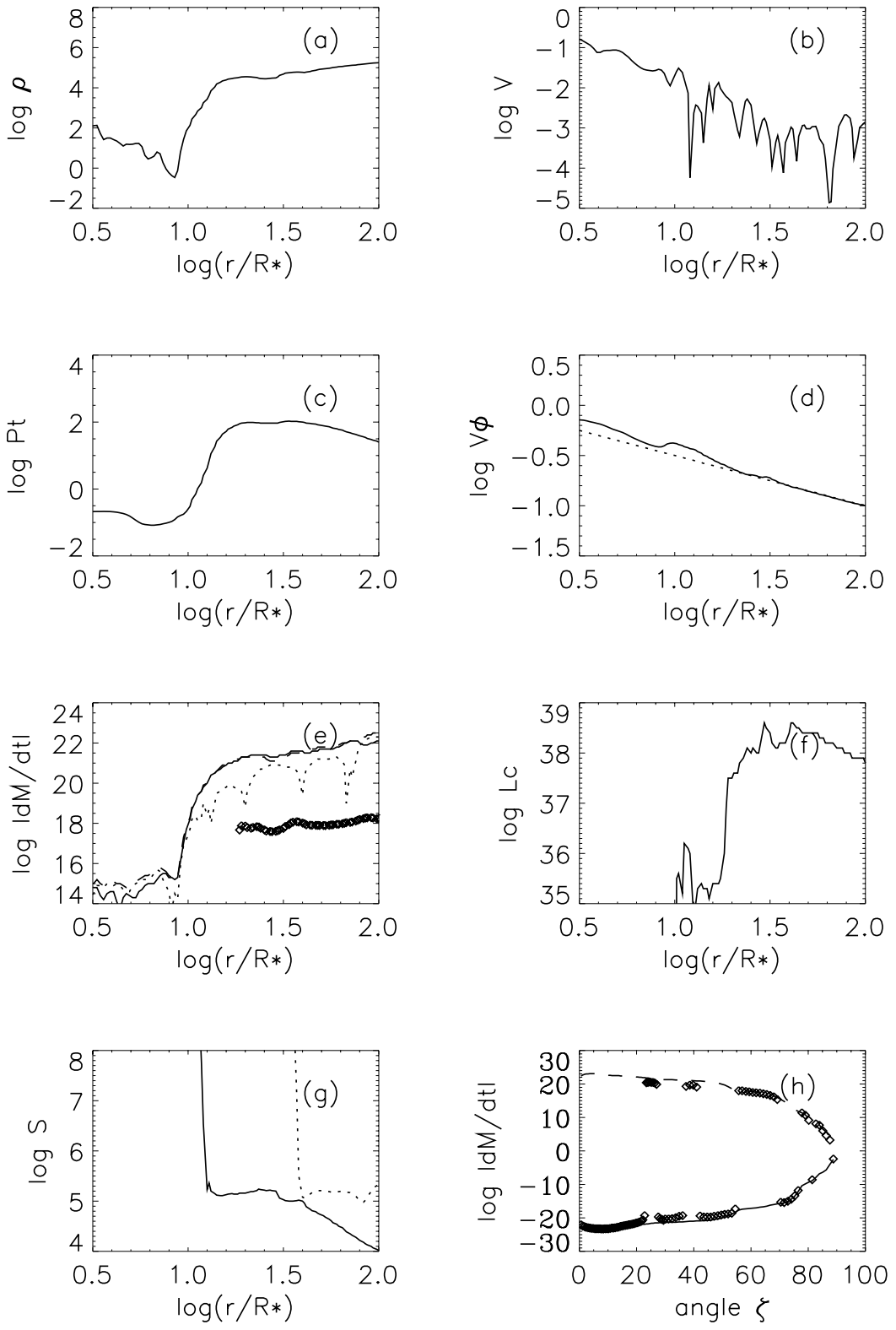

Fig. 7. Radial and angular profiles of the time-averaged flow variables near to the equatorial plane for model BH-1: (a) density ρ, (b) radial velocity v, (c) total pressure $P_{\rm t}$, (d) rotational velocity v_φ, (e) four radial mass-flux rates $\dot{M}(r)$, (f) convective luminosity $L_{\rm c}$, (g) entropy S, and (h) angular profiles of three mass-flux rates $\dot{M}(\zeta)$ (see text in detail).

advection-dominated zone, in which the net mass-inflow rate, $\dot{M}_{\rm in}$, is small, and an outer convection-dominated zone, in which $\dot{M}_{\rm in}$ increases with increasing radii. From figures 6 and 7, we can see that the accretion flow apparently consists of two such zones. The transition radius, $r_{\rm tr}$, between the zones is $\sim 10R_*$ ($=20r_{\rm g}$), which is larger than $10r_{\rm g}$ in Stone and Pringle (2001), but smaller than 30–$50r_{\rm g}$ in Abramowicz et al. (2001). At $r \lesssim r_{\rm tr}$, convection is absent and the mass-inflow rate is very small. On the other hand, at $r \gtrsim r_{\rm tr}$ the flow is convectively turbulent and accretes slowly.

From figure 7, we have rough approximations of $\rho \propto r$, $P_{\rm t} \propto r^{-0.85}$, $v_\varphi \propto r^{-1/2}$, and $\dot{M}_{\rm in} \propto r$. The angle-averaged variables are averaged over twenty mesh points between $0 \le \zeta \le 12°$. However, it should be noticed that some variables, such as the entropy, may be considerably dependent on ζ, as is found in figure 7g, which shows $S(\zeta \sim 0) \propto r^{-1.6}$ at $r/R_* \gtrsim 12$ but $S(\zeta = 42°) \sim$ constant at $r/R_* \gtrsim 40$. The entropies at $\zeta = 0°$ and 42° sharply increase at $r/R_* \lesssim 12$ and 40, respectively, which lie almost in the disk surface, because of $S \propto T^3/\rho$ in the radiation-dominated region. The entropy profiles within the disk show equi-contours vertical to the equator and considerable radial gradients near to the disk mid-plane, but radial equi-contours in the upper disk.

Other radial profiles are compared with those of (1) $\rho \propto r^{-1/2}$, $P_{\rm t} \propto r^{-3/2}$, $v \propto r^{-1/2}$, and $\dot{M}_{\rm in} \propto r$ for a self-similar solution (Igumenshchev, Abramowicz 1999; Narayan et al. 2000), (2) $\rho \propto r^{-1/2}$, $P_{\rm t} \propto r^{-3/2}$, $v = 0$, $v_\varphi \propto r^{-1/2}$, and $\dot{M}_{\rm in} = 0$ for a non-accretion convective envelope solution (Narayan et al. 2000; Quataert, Gruzinov 2000), and (3) $\rho \propto r^0$, $P_{\rm t} \propto r^{-1}$, $v \propto r^{-1}$, and $\dot{M}_{\rm in} \propto r$ for hydrodynamical simulations with $\nu = 10^{-2}\rho$ (Stone et al. 1999). The large differences of the profiles between ours and theirs are the density profile with $\rho \propto r$ in model BH-1. However, it is natural that the very luminous disk like model BH-1 would have such density inversion profile, because the initial Shakura–Sunyaev disk has $\rho \propto r^{3/2}$ and $P_{\rm t} \propto T^4 \propto r^{-3/2}$ in the inner region of the disk, where the radiation-pressure and electron scattering are dominant (Shakura, Sunyaev 1973). However, the self-similar solutions and other simulations are considered under a negligible radiation-pressure condition.

In figure 6, we remark on the existence of an "accretion zone" just below the disk boundary, but above the top of the convective zones. This accretion zone is also found in Eggum et al. (1985, 1988). At $r > r_{\rm tr}$, roughly half the mass at any time at any radius will be flowing in and flowing out, respectively, and the mass-inflow rate, $\dot{M}_{\rm in}$, balances the mass-outflow rate, $\dot{M}_{\rm out}$. Near to the transition region, by way of the convective zones and the accretion zone, matter is accreted towards the equatorial plane. The accreting matter, which is carried to the transition region by convection, partly diverts into the high-velocity jets and partly flows into the inner advection-dominated zone. Thus, the rate of mass-flow swallowed into the black hole is as very small as $\sim 5 \times 10^{14}\,{\rm g\,s^{-1}}$, because the densities near the inner boundary are as very small as $\sim 10^{-14}$–$10^{-26}\,{\rm g\,cm^{-3}}$, although the velocities are as very large as $-0.3\,c$ to $-0.6\,c$. On the other hand, the mass-loss rate of the jets at the outermost boundary is $\sim 4 \times 10^{18}\,{\rm g\,s^{-1}}$, which is one order of magnitude smaller than the input accretion rate, $\dot{M}_*$, whereas the mass-outflow rate, $\dot{M}_{\rm out}$, through the outermost disk boundary is as large as the input accretion rate. We notice that the radial mass-outflow rate in the jets region increases with radii, roughly as $\dot{M}_{\rm jet} \propto r$ in figure 7e, analogously with other mass-flow rates $\dot{M}_{\rm in}(r)$ and $\dot{M}_{\rm out}(r)$, and furthermore that the ζ-direction net mass-outflow rate $\dot{M}_{\rm p}$ in figure 7h changes from its negative value to a positive value of $\sim 10^{18}\,{\rm g\,s^{-1}}$ at $\zeta \sim 56°$, where the angle position corresponds to the boundary between the disk and the jets region. After crossing the boundary, $\dot{M}_{\rm p}$ decreases abruptly because the outflow gas from the disk surface is strongly bent toward the radial direction due to the dominant radial radiation-pressure force in the high-velocity region.

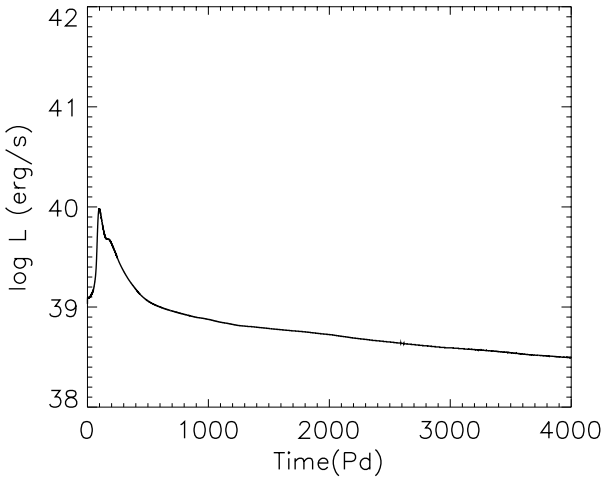

Fig. 8. Time evolution of the luminosity L for model BH-2.

This shows that a considerable disk wind is generated in the upper disk and is incorporated into the high-velocity flow. Therefore, a part of the convective flow escapes from the whole system as the disk wind and the other may always remain in convective circulations through the disk. Thus far, we expect that the mass-loss rate of the jets at great large radii will become much larger than the value of $4 \times 10^{18}\,{\rm g\,s^{-1}}$ calculated here.

4.2. Model BH-2 with $\alpha = 0.1$

The shape of the initial disk is very similar to that of model BH-1, but the densities and the temperatures on the disk mid-plane in model BH-2 are more than one order of magnitude and by a few factors larger than those in model BH-1, respectively. Figure 8 shows the time evolution of the luminosity for model BH-2. The luminosity, $2.5 \times 10^{38}\,{\rm erg\,s^{-1}}$, at the final phase, $t = 4365P_{\rm d}$, is one order of magnitude smaller than that in model BH-1, and $L/L_{\rm E}$ is ~ 0.16.

This model shows very different time evolutions from model BH-1. Mass ejection from the disk surface first begins at the innermost region of the disk, and subsequently occurs at the outer part of the disk. Although the ejected gas is blown off partly through the outer boundary, it accumulates in the outer part of the disk with increasing time. Finally, the disk becomes fatter at the outer part than the initial disk. The obtained accretion disk is geometrically thick as $H/r \sim 0.2$, and has an opening angle of $\sim 10°$ to the equatorial plane.

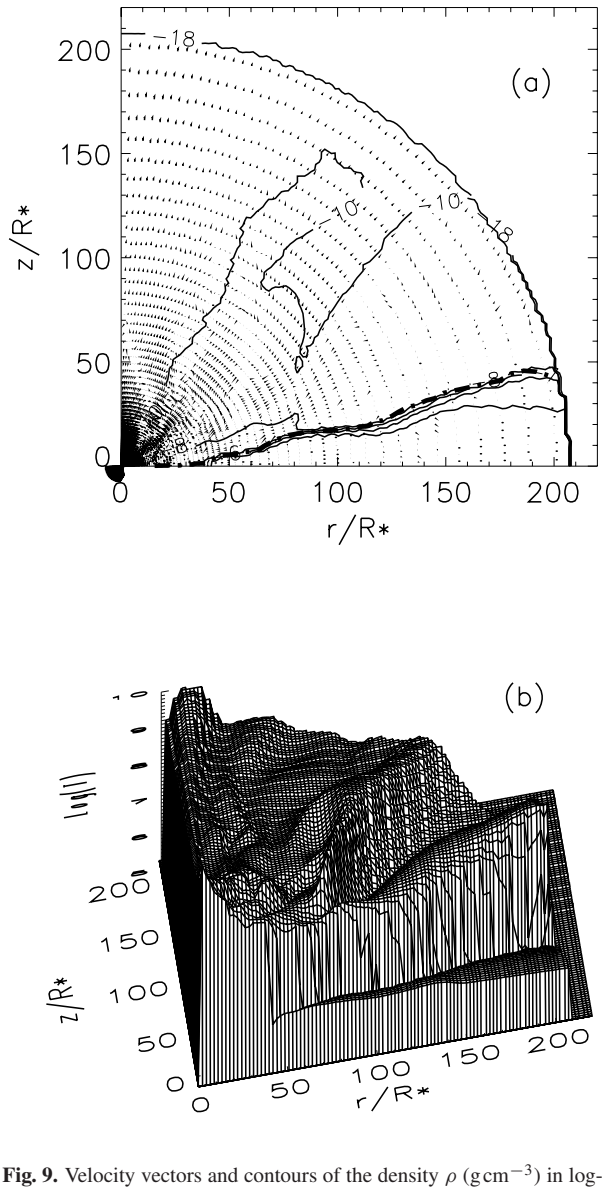

Fig. 9. Velocity vectors and contours of the density ρ (g cm^{-3}) in logarithmic scale (a) and a bird's-eye view of the gas temperature T (K) (b) on the meridional plane at $t = 4365 P_{\rm d}$ for model BH-2, where the thick dot-dashed line in (a) shows the disk boundary between the disk and the surrounding atmosphere, and the flow vectors are denoted in the same units as in figure 3a.

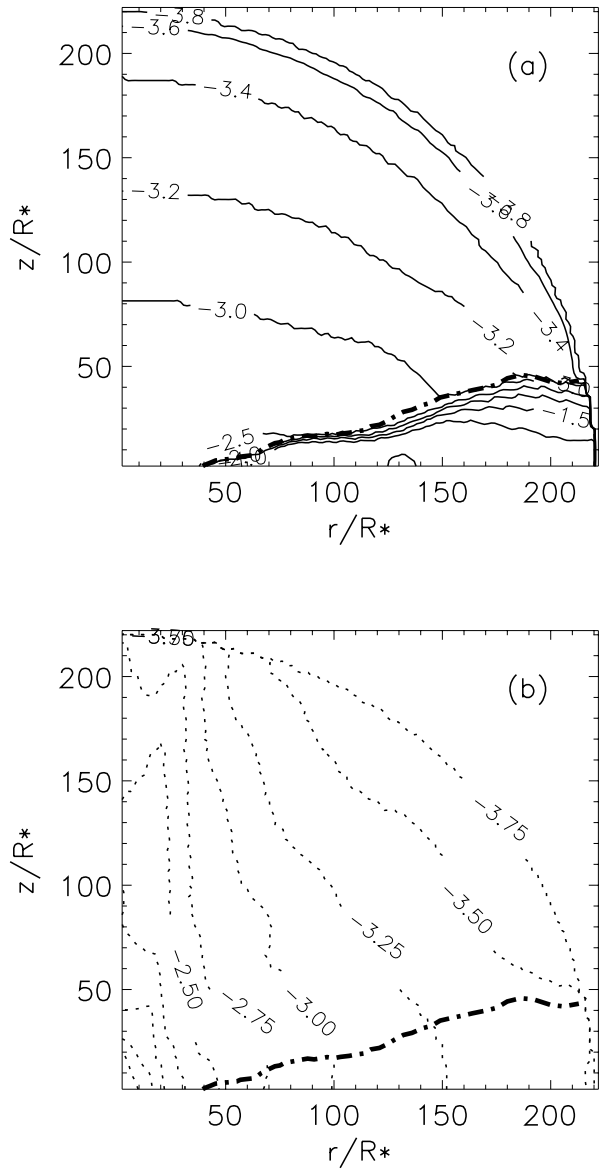

Fig. 10. Contours of the radiation energy density (a) and the angular-velocity Ω (b) on the meidional plane at $t = 4365 P_{\rm d}$ for model BH-2 with the same units as in figure 4.

Figure 9 shows the density contours with velocity vectors (a) and a bird's-eye view of the temperature contours (b) on the meridional plane at the final phase. The thick dot-dashed line in figure 9a shows the disk boundary between the disk and the surrounding atmosphere. In this figure we never find any relativistic jets along the rotational axis as is found in model BH-1. The temperatures and densities at the atmospheric region around the disk are as hot as $\sim 10^8$–10^{10} K and as low as $\sim 10^{-9}$–10^{-12} g cm^{-3}, respectively, but the outflow velocities are not very large in model BH-2, where the maximum velocity is $\sim 0.07\,c$ near the rotational axis. Large gradients of the density and the temperature across the disk boundary are also found in figures 9a and b.

Figure 10 shows contours of the radiation energy density E_0 (a) and the angular velocity Ω (b) on the meridional plane at $t = 4365 P_{\rm d}$ with the same units as in figure 4. The disk is nearly Keplerian throughout its whole shape, but the atmospheric region above the disk shows non-Keplerian angular velocities. There also appear convective cells at $15 \lesssim r/R_* \lesssim 50$. The densities and temperatures at $r/R_* \lesssim 10$ on the disk mid-plane become more rarefied and much hotter than those in the initial disk, respectively, and a spherical high-temperature region is formed around here. The densities near the inner boundary are much larger, $\sim 10^{-9}$–10^{-10} g cm^{-3}, than those in model BH-1. The rate of the resultant mass-inflow swallowed into the black hole is much larger, $\sim -1.4 \times 10^{16}$ g s^{-1}, than the $\sim -5 \times 10^{14}$ g s^{-1} in model BH-1, but is negligibly small compared with the input accretion rate.

The disk features obtained here are interpreted, rather, under

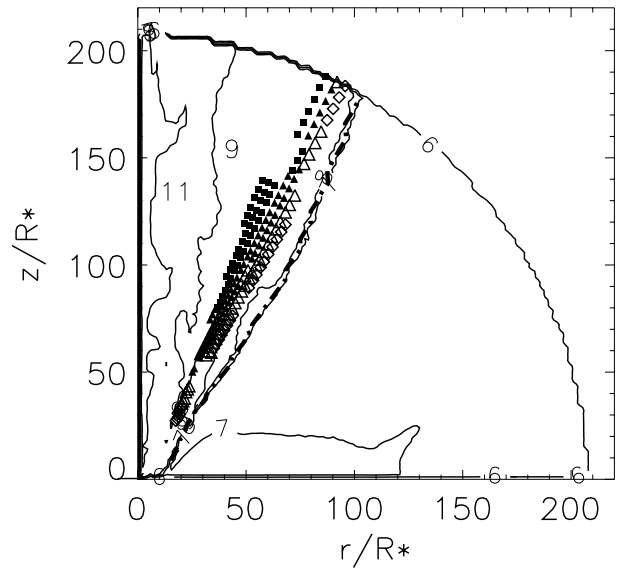

Fig. 11. Distribution of mesh points contributed most to the total X-ray emission of iron lines at $t = 3577 P_{\rm d}$ for model BH-1, where the disk boundary (thick dot-dashed line) and the temperature contours of $\log T = 7$, 8, 9, and 11 (lines) are also plotted. The diamonds, triangles, filled triangles, and filled squares denote the mesh points with different flow velocities of $\sim 0.10c$, $0.13c$, $0.17c$, and $0.20c$, respectively. Only mesh points with emissivity of more than a hundredth of the maximum emissivity in the optically-thin region are plotted here.

a category of the standard disk model, though the disk is geometrically thick. The result of model BH-2 describes that the concept of relativistic jets expected for the super-Eddington accretion disks around black holes must be modified under the α-model of viscosity, i.e., for the case of strong kinematic viscosity, there exists no relativistic and well-collimated outflow jet, even in the super-Eddington accretion disks. Though the densities and temperatures at the atmosphere around the disk are in the range of those required for the X-ray jets of SS 433, the maximum outflow velocity is at most $\sim 0.07c$ and the flows are not well collimated anywhere. Therefore, we can not expect X-ray emission lines with a definite Doppler shift of $0.26c$ observed in SS 433, and conclude that model BH-2 is unfavorable for SS 433.

4.3. X-ray Emitting Region of Iron Lines

For a Maxwellian distribution of the electron velocities, the power emitted per unit volume due to excitations of level n' of ion Z in the ground state n by electron collision is given by

$$\frac{dP}{dV} = 1.9 \times 10^{-16} T^{-1/2} \overline{\Omega} \left(\frac{\Delta E}{I_{\rm H}} \right) \times e^{-\Delta E/kT} N_{\rm e} N_Z \ {\rm erg\ cm^{-3}\ s^{-1}}, \quad (18)$$

where ΔE, $I_{\rm H}$, k, $N_{\rm e}$, N_Z, and $\overline{\Omega}$ are the excitation energy between the n and n' levels, the ionization potential of hydrogen, the Boltzmann constant, the number density of electrons, the number density of ion Z, and the effective average of collision strength Ω, respectively (Blumenthal, Tucker 1974). The red- and blue-shifted highly ionized iron lines, Fe XXV K_α and Fe XXVI K_α, are clearly seen in all of the observed X-ray spectra of SS 433 (Kotani et al. 1996). Typically, focusing on the Fe XXV K_α line, we calculated the total power emitted by the iron lines through the optically-thin region.

Figure 11 shows the mesh points which contributed most to the total X-ray power of the iron lines at $t = 3577 P_{\rm d}$ for model BH-1, where only mesh points with emissivity of more than a hundredth of the maximum emissivity in the optically-thin region are indicated by the triangles, squares, filled triangles, and filled squares, which show different flow velocities of $\sim 0.10c$, $0.13c$, $0.17c$, and $0.20c$ at the mesh points, respectively. The influences of photoionization and photoexcitation by the intense radiation field in the innermost region were not taken account of here. If these effects are considerable, the results in figure 11 may be invalid. In this respect, we mention that Brinkmann and Kawai (2000) showed the effect of photoionization on the iron-line flux ratio to be relatively small, using their jets model of SS 433 and assuming that the emission at the base of the jets is given by a black body, where the temperatures and densities (4×10^8 K and 10^{-9}–10^{-10} g cm^{-3}, respectively) used in their model are of the same orders as those in the marked region in figure 11.

We notice that the emitting region of the iron lines in figure 11 is confined into a narrow region at $63^\circ \lesssim \zeta \lesssim 68^\circ$ just outside the disk boundary, and that the high-velocity gas in the funnel region would never contribute to the X-ray line emission, because the densities in the region are more than ten orders of magnitude smaller than those in the narrow region, regardless of the high-temperatures in the funnel region. The accretion disk, itself, does not contribute to the X-ray line emission, because the temperatures are as low as $\sim 10^6$–10^7 K and its emissivity decreases exponentially as $e^{-\Delta E/kT}$ in spite of the high densities in the disk. Therefore, we consider that the unique velocity, $0.26c$, of SS 433 would be attributed to the effective velocity in the above emitting region of the iron lines.

5. Discussion

5.1. Comparison with Other Results

Our present results are compared with those of a super-Eddington black hole model by Eggum et al. (1985, 1988), who considered a black hole of $M_* = 3 M_\odot$ and $\dot{M}_* = 4 \dot{M}_{\rm E}$ and used the flux-limited diffusion approximation for the radiation transport. The black hole mass is by a factor 3 smaller than ours, but the input accretion rate is the same as ours. They used a constant kinematic viscosity, $\nu = 1.5 \times 10^{15}$ cm^2 s^{-1}, instead of the usual α-model for viscosity.

There exist some qualitatively important and common results between our model BH-1 and their model, such as the relativistic funnel jets, the geometrically thick disk, the accretion zone, and the remarkable convective phenomena in the disk. In their results, the flows between the disk and the rotational axis are accelerated to relativistic velocities due to the radiation-pressure force. The collimation angle of the jets to the rotational axis is also as large as $\sim 30^\circ$ in model BH-1. The mass-outflow rate obtained by Eggum et al. (1985, 1988) is three orders of magnitude smaller than the input accretion rate, $\dot{M}_*$, and accordingly the estimated $\dot{M}_{\rm loss}$ of SS 433. On the other hand, the mass-outflow rate from the high-velocity jets in model BH-1 is much larger than that in Eggum et al.,

although it is one order of magnitude smaller than the estimated value in SS 433. Most of the accreting matter in Eggum et al. (1985, 1988) is swallowed into the central black hole through the inner boundary, but the mass-flow rate into the black hole in our model is negligibly small compared with the input accretion rate. The differences in the numerical results may be attributed to the high kinematic-viscosity, ν, of $1.5\times10^{15}\,\mathrm{cm^2\,s^{-1}}$ in Eggum et al. (1985, 1988), which is more than two orders of magnitude larger than those at $r/R_* \lesssim 20$ and at $r/R_* \gtrsim 50$, respectively, on the disk mid-plane in model BH-1.

5.2. *Convection-Dominated Accretion Flows with Small α*

As an alternative model to ADAFs models, since Narayan and Yi (1994), Blandford and Begelman (1999) proposed advection-dominated inflow–outflow solutions (ADIOS) which include a powerful wind that carries away mass, angular momentum, and energy from the accreting gas. A typical case with appropriate parameters shows that only a small fraction of the mass supplied will reach the black hole, accompanying a disk wind. In relation to these ADAFs, Narayan et al. (2000), Quataert and Gruzinov (2000), and Abramowicz et al. (2001) developed the convection-dominated accretion flows (CDAFs) or a 'convective envelope solution'. The CDAFs models assume that the convective energy transport is primarily directed radially outward through the disk, but with no outflows, whereas in the ADIOS models the convective energy transport has a large ζ-direction component toward the disk surface at high latitudes, which will drive strong outflows.

The initial Shakura–Sunyaev disk for model BH-1 is originally unstable to convection, since the entropy, $S \propto T^3/\rho$, in the radiation-pressure-dominant inner disk falls abruptly with increasing Z. Convection tends to establish an isentropic structure along the Z-axis, which results in equi-contours of entropy vertical to the equator near to the disk mid-plane in model BH-1. The convective flows accompanied by a large mass-outflow from the disk surface may be relevant to the ADIOS models. On the other hand, large negative radial gradients of the entropy near to the mid-plane in model BH-1 also induce large convective energy transport directed radially outward through the disk, as can be seen in figures 7f and g. As a result, the accretion flows in model BH-1 may be dominated by a ADIOS model and also a CDAFs model.

The convective envelope solution, which is special one of the CDAFs, was addressed by Narayan et al. (2000) and Quataert and Grunizov (2000). The convective envelope solution expresses that $v \sim 0$ and the viscous dissipation rate, Q^+, is ~ 0 because the net shear stress via viscosity and via convection vanishes. This leads to no advection entropy, and thus the divergence of the convective energy flux vanishes from the energy equation, that is, $F_\mathrm{c}(r) \propto r^{-2}$. The relation $F_\mathrm{c} \propto r^{-2}$ is also derived from the definition $F_\mathrm{c} = -3\alpha(c_\mathrm{s}^2/\Omega_\mathrm{K})\rho T\, dS/dr$ (Narayan et al. 2000) and using the radial profiles of $\rho \propto r$ and $P_\mathrm{t} \propto r^{-0.85}$ in figure 7, where c_s is the sound speed. Figure 7f shows roughly $L_\mathrm{c} \sim$ constant in the outer region; accordingly, $F_\mathrm{c} \propto r^{-2}$ if F_c is independent of ζ. Even for net zero stress, the negative radial gradient of the entropy would be maintained if the high-entropy gas is lost in a considerable disk wind, as is found in model BH-1. Accordingly, model BH-1 may possess a circumstance near the convective envelope solution, although the mean radial velocity is not exactly zero. In this respect, further knowledge of the actual mechanism of the angular momentum transport by convection is required.

Abramowicz and Igumenshchev (2001) suggest that CDAFs have a significant outward energy flux carried by convection, with a luminosity of $L_\mathrm{c} = \epsilon_\mathrm{c}\dot{M}c^2$, where the efficiency, ϵ_c, is $\sim 3\times10^{-3}$–10^{-2}, independently of the accretion rate, and the radiative output comes mostly from the convective part. In model BH-1, the convective luminosity, L_c, near the outer boundary is $\sim 5\times10^{37}\,\mathrm{erg\,s^{-1}}$, which is far smaller than the radiative luminosity, L ($\sim 1.6\times10^{39}\,\mathrm{erg\,s^{-1}}$) at $t = 3577\,P_\mathrm{d}$; this corresponds to $\epsilon_\mathrm{c} \sim 10^{-3}$, which agrees with that by Abramowicz and Igumenshchev (2001). However, the luminosity, L, comes mostly from the innermost hot region at $r \sim r_\mathrm{tr}$ through the optically-thin high-velocity region, instead of the convective-dominated disk. Indeed, $\dot{M}_\mathrm{a}GM/r_\mathrm{tr}$ gives $2\times10^{39}\,\mathrm{erg\,s^{-1}}$, which corresponds well to L, roughly using $\dot{M}_\mathrm{a}(r_\mathrm{tr}) \sim 10^{20}\,\mathrm{g\,s^{-1}}$ and $r_\mathrm{tr} \sim 20\,r_\mathrm{g}$ from figure 7.

Finally, we emphasize that most of the simulations and theoretical models so far have been done on thin accretion disks without radiation, and that it is not still clear whether these results are valid for the much thicker and radiation-pressure-dominant disks. Further theoretical studies on the radiation-pressure dominant ADAFs and CDAFs are required.

5.3. *Relativistic Jets, Collimation, and Mass-Outflow Rate*

Observations of SS 433 show many emission lines of heavy elements, such as Fe and Ni, which denote the unique red and blue Doppler shifts of $0.26\,c$ in the X-ray region. The collimation angle of SS 433 jets seems to be as small as 0.1 radian (several degrees) (Margon 1984). Any models for SS 433 must explain the characteristics of these emission lines. The unique velocity, $0.26\,c$, may be reasonably explained in terms of the relativistic velocities at a confined region just outside of the upper disk boundary, which lies between the funnel wall and the disk, as is found in model BH-1. The velocity $0.26\,c$ is not an inherent velocity of SS 433 like an orbital velocity in the binary system, but is a result of the super-Eddington accretion disk.

The collimation angle, $\sim 30°$, of the high-velocity jets in model BH-1 is rather large compared with the value of ~ 0.1 radian expected for SS 433 jets. If the calculated high-velocity jets should be truly confined to a small angle of ~ 0.1 radian from the rotating axis, we need a collimation mechanism operating outside the present computation grids, or some mechanism, such as magnetohydrodynamical collimation, which is not considered here. This problem remains open, although there exist some discussions that the jets of SS 433 may not be well collimated, as is inferred from the line profiles, and that the 0.1 radian jet may not be consistent with the X-ray observations of SS 433 (Eggum et al. 1988).

Hydrodynamical modeling of the jets combined with recent X-ray observations reveals temperatures of $(6$–$8)\times10^8\,\mathrm{K}$, particle densities of between 5×10^{11}–$5\times10^{13}\,\mathrm{cm^{-3}}$ at the base of the jets, and the length of the X-ray jets being $\gtrsim 10^{10}\,\mathrm{cm}$ (Brinkmann et al. 1991; Brinkmann 1993; Kotani et al. 1996). These temperatures and densities required for the X-ray jets qualitatively agree with those at the high-velocity region between the funnel wall and the disk boundary in model BH-1.

The X-ray emitting region observed in SS 433 would be in the range of $r = 10^{10}$–10^{12} cm (Kotani et al. 1996), which far exceeds the present computational domain. The high-velocity jets region in model BH-1 would probably extend up to $r \sim 10^{12}$ cm. Additionally, from the characteristics of the results given in figure 3, we expect that such an extended high-velocity region would have temperatures and densities of $\sim 10^8$ K and $\sim 10^{-12}$–$10^{-10}\,\mathrm{g\,cm^{-3}}$. Although the mass-loss rate ($4 \times 10^{18}\,\mathrm{g\,s^{-1}}$) of the jets in model BH-1 is one order of magnitude smaller than the mass-loss rate ($\geq 3 \times 10^{19}\,\mathrm{g\,s^{-1}}$) estimated in SS 433, we speculate that the actual calculated mass-loss rate at large radii may become comparable to the observed one, because the jets mass-flux would increase due to the wind gas from the disk at large radii. In such a case, we may have a problem that the jets gas may slow down below $0.26\,c$ if the enhanced region of the jets mass-flux is too far from the present computational domain. Alternatively, the super-Eddington models with a much larger input accretion rate, $\dot{M}_*$, than the present value, $4\dot{M}_{\mathrm{E}}$, may be responsible for a mass-loss rate comparable to $\sim 10^{20}\,\mathrm{g\,s^{-1}}$.

5.4. *Central Object of SS 433*

Whether the central object of SS 433 is a black hole or a neutron star remains unsolved even at present, because we have not yet obtained any decisive evidence of a central source mass. From some observational and theoretical estimates of a massive mass and its too high energetics of SS 433, many astrophysicists seem to favor a black-hole hypothesis of SS 433 (Leibowitz et al. 1984; Fabrika, Bychkova 1990; Cherepashchuk 1993; Fukue et al. 1998; Hirai, Fukue 2001), while some people suggest that the compact object is a neutron star, from the viewpoint of a theoretical model and observations of the He II line (Begelman, Rees 1984; D'Odorico et al. 1991; Zwitter et al. 1993).

In this respect, our present results are also compared with those of a neutron-star model by Okuda and Fujita (2000) with $M_* = 1.4\,M_\odot$, $R_* = 10^6$ cm, and a mass accretion rate ($\dot{M}_*$) of 10^{20} g s^{-1}, which corresponds to $\sim 100\dot{M}_{\mathrm{E}}$ for a neutron star. The viscosity parameter, $\alpha = 10^{-3}$, used is the same as that in model BH-1. The characteristic features in model BH-1 are also found in this neutron-star model, where there appear a high-velocity jet region with a collimation angle of $\sim 10^\circ$ to the rotational axis, the existence of a confined X-ray emitting region of iron lines in the high-velocity region, a geometrically-thick disk with an opening angle of 80° to the equatorial plane, a mass-loss rate far less than 10^{20} g s^{-1}, and convective motions in the inner disk. Regarding the collimation angle, the neutron-star model with a smaller angle $\sim 10^\circ$ may be favorable for SS 433. However, except for this point, there is no intrinsic or large quantitative difference between the neutron-star model and the black-hole model; that is, we could not find any decisive proof for these objects as a candidate of SS 433.

5.5. *Assumption of the Flux-Limited Diffusion Approximation*

The radiation transport was treated here as an approximation of flux-limited diffusion. The flux limiter, λ, and the Eddington factor, f_{E}, used in the approximation are given from the empirical formulas fitted to some stellar atmosphere models (Kley 1989). Recently, Turner and Stone (2001) addressed that the flux-limited diffusion approximation (FLD) is less accurate when the flux has a component perpendicular to the gradient in radiation energy density, and in optically-thin regions when the radiation field depends strongly on the angle. The calculations considered in our case typically result in two optical regions, which are the optically-thick disk region and the optically-thin high-velocity region. The flux limiter, λ, is almost $1/3$ in the disk and, contrarily, very small everywhere in the high-velocity region. In an optically-thick disk, FLD is sufficient. On the other hand, in the optically-thin high-velocity region, the radiation fields are highly anisotropic and FLD may be less accurate. The radiation fields in the high-velocity region originate in radiation from the central hot region and the outer disk surface. However, the contours of radiation energy density are almost concentric around the central object. Actually, the radial radiation flux, which is attributed to the central hot region, is one order of magnitude larger than the radiation flux normal to the disk surface. As a result, we consider that FLD in our code would not result in any serious influences on the whole dynamics of the flows and the total luminosity; still, this problem should be checked with a more accurate method in future improvements of the numerical code.

6. Conclusions

We examined highly super-Eddington black-hole models for SS 433, based on two-dimensional hydrodynamical calculations coupled with radiation transport. A model with a small viscosity parameter, $\alpha = 10^{-3}$, shows that a geometrically- and optically-thick convection-dominated disk with a large opening angle of $\sim 60^\circ$ to the equatorial plane and rarefied, very hot, and optically-thin high-velocity jets region around the disk are formed. The thick accretion flow near to the equatorial plane consists of two different zones: an inner advection-dominated zone, in which the net mass-inflow rate, $\dot{M}_{\mathrm{in}}$, is very small, and an outer convection-dominated zone, in which $\dot{M}_{\mathrm{in}}$ increases with increasing radii. The high-velocity region along the rotating axis is divided into two characteristic regions by the funnel wall, a barrier where the effective potential due to the gravitational potential and the centrifugal one vanishes. A confined region in the high-velocity jet region just outside of the photospheric disk boundary would be responsible for the observed X-ray iron emission lines with a Doppler shift of $0.26\,c$. However, from this model, we can not obtain a small collimation degree of ~ 0.1 radian of the jets and a sufficient mass-outflow rate of the jets comparable to $\sim 10^{20}\,\mathrm{g\,s^{-1}}$, as is expected for SS 433. These problems still remain open. On the other hand, from a model with a large $\alpha = 0.1$, we find a geometrically and optically thick quasi-Keplerian disk with an opening angle of $\sim 10^\circ$ to the equatorial plane, whereas the disk is far thinner than the disk with $\alpha = 10^{-3}$. This model may be unfavorable to SS 433 because we never find relativistic jets with $\sim 0.2\,c$ here. Further investigations of the super-Eddington models with other model parameters and over a wider range of the computational domain ($r \sim 10^{12}$ cm) may give some key to the open problems.

The author gratefully thanks Dr. D. Molteni for his useful discussions of the numerical method and the results,

and also the referee for many useful comments concerning the advection-dominated and the convection-dominated accretion flows. Numerical computations were carried out at the Information Processing Center of Hokkaido University of Education.

References

Abramowicz, M. A., & Igumenshchev, I. V. 2001, ApJ, 554, L53
Abramowicz, M. A., Igumenshchev, I. V., Quataert, E., & Narayan, R. 2001, preprint (astro-ph/0110371)
Begelman, M. C., & Rees, M. J. 1984, MNRAS, 206, 209
Bisnovatyi-Kogan, G. S., & Blinnikov, S. I. 1977, A&A, 59, 111
Blandford, R. D., & Begelman, M. C. 1999, MNRAS, 303, L1
Blumenthal, G. R., & Tucker, W. H. 1974, in X-Ray Astronomy, ed. R. Giacconi & H. Gursky (Dordrecht: Reidel), 99
Brinkmann, W. 1993, in Stellar Jets and Bipolar Outflows, ed. L. Errico & A. A. Vittone (Dordrecht: Kluwer), 193
Brinkmann, W, & Kawai, N. 2000, A&A, 363, 640
Brinkmann, W., Kawai, N., Matsuoka, M., & Fink, H. H. 1991, A&A, 241, 112
Calvani, M., & Nobili, L. 1983, in Astrophysical jets, ed. A. Ferrari & A. G. Pacholczyk (Dordrecht: Reidel), 189
Cherepashchuk, A. M. 1993, in Stellar Jets and Bipolar Outflows, ed. L. Errico & A. A. Vittone (Dordrecht: Kluwer), 179
D'Odorico, S., Oosterloo, T., Zwitter, T., & Calvani, M. 1991, Nature, 353, 329
Eggum, G. E., Coroniti, F. V., & Katz, J. I. 1985, ApJ, 298, L41
Eggum, G. E., Coroniti, F. V., & Katz, J. I. 1988, ApJ, 330, 142
Fabrika, S. N., & Bychkova, L. V. 1990, A&A, 240, L5
Fujita, M., & Okuda, T. 1998, PASJ, 50, 639
Fukue, J. 1982, PASJ, 34, 163
Fukue, J. 1996, PASJ, 48, 631
Fukue, J., Obana, Y., & Okugami, M. 1998, PASJ, 50, 81
Hirai, Y., & Fukue, J. 2001, PASJ, 53, 679
Icke, V. 1980, AJ, 85, 329
Icke, V. 1989, A&A, 216, 294
Igumenshchev, I. V., & Abramowicz, M. A. 1999, MNRAS, 303, 309
Kato, S., Fukue, J., & Mineshige, S. 1998, Black Hole Accretion Disks (Kyoto: Kyoto University Press)
Katz, J. I. 1980, ApJ, 236, L127
King, A. R., & Begelman, M. C. 1999, ApJ, 519, L169
Kley, W. 1989, A&A, 208, 98
Kley, W., & Lin, D. N. C. 1996, ApJ, 461, 933
Kotani, T., Kawai, N., Matsuoka, M., & Brinkmann, W. 1996, PASJ, 48, 619
Leibowitz, E. M., Mazeh, T., & Mendelson, H. 1984, Nature, 307, 341
Levermore, C. D., & Pomraning, G. C. 1981, ApJ, 248, 321
Lipunov, V. M., & Shakura, N. I. 1982, SvA 26, 386
Lynden-Bell, D. 1978, Phys. Scr., 17, 185
Margon, B. 1984, ARA&A, 22, 507
Meier, D. L. 1982, ApJ, 256, 706
Milsom, J. A., & Taam, R. E. 1997, MNRAS, 286, 358
Molteni, D., Ryu, D., & Chakrabarti, S. K. 1996, ApJ, 470, 460
Narayan, R., Igumenshchev, I. V., & Abramowicz, M. A. 2000, ApJ, 539, 798
Narayan, R., & Yi, I. 1994, ApJ, 428, L13
Okuda, T., & Fujita, M. 2000, PASJ, 52, L5
Okuda, T., Fujita, M., & Sakashita, S. 1997, PASJ, 49, 679
Paczyński, B., & Wiita, P. J. 1980, A&A, 88, 23
Papaloizou, J. C. B., & Stanley, G. Q. G. 1986, MNRAS, 220, 593
Quataert, E., & Gruzinov, A. 2000, ApJ, 539, 809
Shakura, N. I., & Sunyaev, R. A. 1973, A&A, 24, 337
Sikora, M., & Wilson, D. B. 1981, MNRAS, 197, 529
Stone, J. M., & Pringle, J. E. 2001, MNRAS, 322, 461
Stone, J. M., Pringle, J. E., & Begelman, M. C. 1999, MNRAS, 310, 1002
Tajima, Y., & Fukue, J. 1998, PASJ, 50, 483
Turner, N. J., & Stone, J. M. 2001, ApJS, 135, 95
Zwitter, T., D'Odorico, S., Oosterloo, T., & Calvani, M. 1993, in Stellar Jets and Bipolar Outflows, ed. L. Errico & A. A. Vittone (Dordrecht: Kluwer), 209